applied sciences

MDPI

Article

Deadbeat Predictive Current Control for Surface-Mounted Permanent-Magnet Synchronous Motor Based on Weakened Integral Sliding Mode Compensation

Yongkang Zhang [1,2], Chengsheng Ji [3], Qianliang You [2], Dexin Sun [3,*] and Yuee Xie [1,*]

[1] School of Physics and Electronic Engineering, Jiangsu University, Zhenjiang 212013, China; 2222126014@stmail.ujs.edu.cn
[2] Nantong Academy of Intelligent Sensing, Nantong 226010, China; uniais@uniais.cn
[3] Shanghai Institute of Technical Physics, Chinese Academy of Sciences, Shanghai 200083, China; jichengsheng@mail.sitp.ac.cn
* Correspondence: sundexin@mail.sitp.ac.cn (D.S.); yueex@ujs.edu.cn (Y.X.)

Abstract: Deadbeat predictive current control (DPCC) has excellent dynamics and can achieve current control with less computational effort. However, its control performance relies on the precision of the parameters of the motor. Current static error will be generated and control performance will be decreased when the predictive model parameters do not correspond to the practical parameters of the motor. In this article, a weakened integral sliding mode compensation method is proposed which converts the current error into a voltage compensation term and adds it to the prediction control output to effectively compensate for the steady-state error. In addition, a boundary layer is introduced to weaken the integral so as to solve the problems of integral saturation and overshoot caused by the introduction of the integral term when the error is large. Moreover, weight factors are introduced to optimize the feedback current, which enhances the robustness of the system. In the end, the effectiveness of this method is verified via simulation and experimental results.

Keywords: deadbeat predictive current control (DPCC); weakening integral; error compensation; permanent-magnet synchronous motor (PMSM); robustness

check for updates

Citation: Zhang, Y.; Ji, C.; You, Q.; Sun, D.; Xie, Y. Deadbeat Predictive Current Control for Surface-Mounted Permanent-Magnet Synchronous Motor Based on Weakened Integral Sliding Mode Compensation. *Appl. Sci.* **2023**, *13*, 11678. https://doi.org/10.3390/app132111678

Academic Editor: Tomonobu Senjyu

Received: 25 September 2023
Revised: 19 October 2023
Accepted: 23 October 2023
Published: 25 October 2023

Copyright: © 2023 by the authors. Licensee MDPI, Basel, Switzerland. This article is an open access article distributed under the terms and conditions of the Creative Commons Attribution (CC BY) license (https://creativecommons.org/licenses/by/4.0/).

1. Introduction

Power electronics is rising dramatically at the present time, and permanent-magnet synchronous motors (PMSMs) have come to be widely used in robotics, electric vehicles, the aerospace industry, and other fields owing to their compact structure, high torque-to-current ratio, and efficiency, as well as their power density and fault tolerance [1,2]. As the innermost loop of the three-loop cascade system of current, speed, and position, the current loop plays a crucial role [3]. Therefore, a lot of studies have proposed methods to optimize current control, such as using proportional integral (PI) control, sliding mode control (SMC), and predictive control, amongst others [4–7].

PI control has been widely used because of its simple structure, simple arithmetic, and easy implementation, but in fact, PMSM control systems are nonlinear, and this method is a linear control algorithm, so it cannot guarantee that the response speed and accuracy will be balanced simultaneously [4,5]. SMC has low sensitivity to parameter variations and disturbances, and it is highly robust. However, discrete control may cause chattering, which decreases the control performance [6].

With the progress of discrete digital control technology and the constant optimization of chip-processing capabilities, predictive control has attracted considerable attention and has been widely researched due to its simple structure and better dynamic performance. Predictive control methods can be classified as deadbeat predictive control (DPC), trajectory predictive control, model predictive control (MPC) [7], etc. The dynamic performance and

control precision of DPCC is excellent, and DPCC, which has a fixed switching frequency and requires only simple computation compared with other current predictive control methods, can be used in combination with space vector pulse-width modulation (SVPWM) to input to the inverter; hence, it is used widely [8]. However, DPCC is sensitive to parameters, and its control performance is associated with the motor parameters in the prediction model. Temperature variations, magnetic saturation, cross coupling [9], and other disturbances lead to motor parameter mismatches, which result in steady-state errors in DPCC, and this is detrimental to the performance of the control.

The available optimization methods that can be used to solve the abovementioned problems associated with DPCC include the model-free control method, parameter identification, disturbance observer compensation, etc. In [8], model-free control combined with a Luenberger disturbance observer is proposed to improve DPCC performance. This proposed method compensates the error by calculating the predictive control voltage and combining the estimated total disturbance with the ultra-local model. In [10], a parameter decoupling identification method is suggested to decouple and reduce the mutual influence between the stator inductance and the flux linkage, and it is optimized using the Kalman algorithm, which is effective in reducing the current steady-state error and harmonic content. In [11], a control method for the online updating of internal relevant parameters is suggested. This method uses an extended Kalman filter to filter the current, which is effective and easily implemented. In [12], a modified reaching law combined with a non-singular terminal sliding mode disturbance observer is used for compensation, and a harmonic compensation term is added to the current control output, which compensates the error and enhances the robustness of the system. In [13], voltage compensation and the elimination of steady-state error are achieved by improving the non-homogeneous disturbance observer, and a power reaching law is designed to make the system converge better. Some researchers have also achieved a boost by improving both the current and the speed loops. In [14], a speed sliding mode controller is designed to enhance the interference immunity while introducing a reaching law to compensate for the DPCC error. In [15], the speed and the current loop are controlled via SMC and DPCC, respectively, with a high-order sliding mode observer estimating and compensating for the disturbance of both, which improves robustness and current-tracking accuracy. Furthermore, an integral can be introduced for error compensation. In [16], the current error integral is introduced, and the parameter of the flux linkage is dynamically adjusted to cancel the error. In [17], a new method that introduces the current error into the control signal through an integral sliding mode term for error compensation is proposed. This method enhances robustness and guarantees the control capability. However, methods that introduce the integral term inevitably cause integral saturation when the error is large, and this affects the system control.

In this article, a weakened integral sliding mode compensation method is proposed for the first time. The method is intended to address the issue of steady-state errors generated by parameter mismatches in conventional DPCC and integral saturation generated by adding an integral term with a large error. This method introduces the concept of a boundary layer, inside of which is the normal integral, and outside of which the integral is weakened to achieve an anti-windup effect. Secondly, weight factors are introduced to reduce the effect of current fluctuation issues resulting from excessive inductance mismatch. Finally, the one-step delay compensation is used to solve the time delay problem in the practical control system. Our simulation and experimental results indicate that the proposed method eliminates the error effectively when the motor parameters mismatch, solves the integral saturation problem, and strengthens the robustness of the system.

This article is structured as follows. Section 2 describes the principles of DPCC with one-step delay compensation and error analysis in case of parameter mismatch. Section 3 shows how to compensate for the error using a weakened integral sliding mode, proves its stability, and introduces the method of adding weight factors to enhance robustness. In Sections 4 and 5, the effectiveness of the proposed algorithm is verified by testing the

current loop and comparing conventional DPCC with the optimized method through simulation and experiment. Finally, Section 6 summarizes this article.

2. DPCC with Delay Compensation

2.1. The Principles of One-Step Delay Compensation DPCC

The voltage mathematical model [18] for a PMSM in a dq-axis rotating coordinate system can be written as follows:

$$\begin{cases} u_d = R_s i_d + L_d \frac{di_d}{dt} - \omega_e L_q i_q \\ u_q = R_s i_q + L_q \frac{di_q}{dt} + \omega_e L_d i_d + \psi_f \omega_e \end{cases} \tag{1}$$

where u_d and u_q represent the dq-axis voltages; L_d and L_q represent the dq-axis inductances; and ψ_f, R_s, and ω_e represent the permanent-magnet flux linkage, the stator resistance of the PMSM, and the electrical angular velocity, respectively.

The d-axis and q-axis inductances are equal in the surface-mounted permanent-magnet synchronous motor (SPMSM) used in this article, and this is written as $L_d = L_q = L_s$. Let us rewrite Equation (1) as a state equation, taking the voltage and current as the state variables in the dq-axis [19]:

$$\begin{bmatrix} \frac{di_d}{dt} \\ \frac{di_q}{dt} \end{bmatrix} = \begin{bmatrix} -\frac{R_s}{L_s} & \omega_e \\ -\omega_e & -\frac{R_s}{L_s} \end{bmatrix} \begin{bmatrix} i_d \\ i_q \end{bmatrix} + \begin{bmatrix} \frac{1}{L_s} & 0 \\ 0 & \frac{1}{L_s} \end{bmatrix} \begin{bmatrix} u_d \\ u_q \end{bmatrix} + \begin{bmatrix} 0 \\ -\frac{\psi_f \omega_e}{L_s} \end{bmatrix} \tag{2}$$

In practice, if the current loop control period is quite short, Equation (2) can be discretized to obtain a current prediction model:

$$\begin{bmatrix} i_d(k+1) \\ i_q(k+1) \end{bmatrix} = F(k) \begin{bmatrix} i_d(k) \\ i_q(k) \end{bmatrix} + G \begin{bmatrix} u_d(k) \\ u_q(k) \end{bmatrix} + H(k) \tag{3}$$

where $F(k) = \begin{bmatrix} 1 - \frac{T_s R_s}{L_s} & T_s \omega_e(k) \\ -T_s \omega_e(k) & 1 - \frac{T_s R_s}{L_s} \end{bmatrix}$, $G = \begin{bmatrix} \frac{T_s}{L_s} & 0 \\ 0 & \frac{T_s}{L_s} \end{bmatrix}$, and $H(k) = \begin{bmatrix} 0 \\ -\frac{T_s \psi_f \omega_e(k)}{L_s} \end{bmatrix}$.

T_s denotes the sampling time of the control system; $i_d(k+1)$ and $i_q(k+1)$ denote the dq-axis predictive currents at the $(k+1)$th moment; $i_d(k)$ and $i_q(k)$ denote the dq-axis feedback currents at the kth moment; $u_d(k)$ and $u_q(k)$ denote the dq-axis predictive voltages at the kth moment; and $\omega_e(k)$ denotes the electrical angular velocity at the kth moment.

In an ideal case, the voltage generated by predictive control can make the practical feedback current follow the reference value at the next moment, namely $i_{dq}(k+1) = i^*_{dq}(k+1)$, where $i^*_{dq}(k+1)$ denotes the dq-axis reference current at the $(k+1)$th moment. From (3), the predictive voltage of the DPCC output at the kth moment is as follows:

$$\begin{bmatrix} u_d(k) \\ u_q(k) \end{bmatrix} = G^{-1} \left\{ \begin{bmatrix} i^*_d(k+1) \\ i^*_q(k+1) \end{bmatrix} - F(k) \begin{bmatrix} i_d(k) \\ i_q(k) \end{bmatrix} - H(k) \right\} \tag{4}$$

However, in practical digital systems, current sampling, program calculation, etc., will cause a time delay [8], such that the practical feedback current cannot follow the reference value at the next moment. Therefore, in this article, DPCC with delay compensation is used to obtain the predictive voltage at the $(k+1)$th moment.

$$\begin{bmatrix} u_d(k+1) \\ u_q(k+1) \end{bmatrix} = G^{-1} \left\{ \begin{bmatrix} i^*_d(k+2) \\ i^*_q(k+2) \end{bmatrix} - F(k+1) \begin{bmatrix} i_d(k+1) \\ i_q(k+1) \end{bmatrix} - H(k+1) \right\} \tag{5}$$

In cases of very short current control periods, the dq-axis reference current and $\omega_e(k)$ can be equivalent to remain constant over adjacent sampling periods, i.e., $i^*_{dq}(k+2) \approx i^*_{dq}(k)$,$\omega_e(k+1) \approx \omega_e(k)$, in which case, (5) can be rewritten as the following:

$$\begin{bmatrix} u_d(k+1) \\ u_q(k+1) \end{bmatrix} = G^{-1}\left\{ \begin{bmatrix} i^*_d(k) \\ i^*_q(k) \end{bmatrix} - F(k) \begin{bmatrix} i_d(k+1) \\ i_q(k+1) \end{bmatrix} - H(k) \right\} \tag{6}$$

A flowchart of delay compensation DPCC is shown in Figure 1, where the predictive currents $i_d(k+1)$ and $i_q(k+1)$ are calculated using (3).

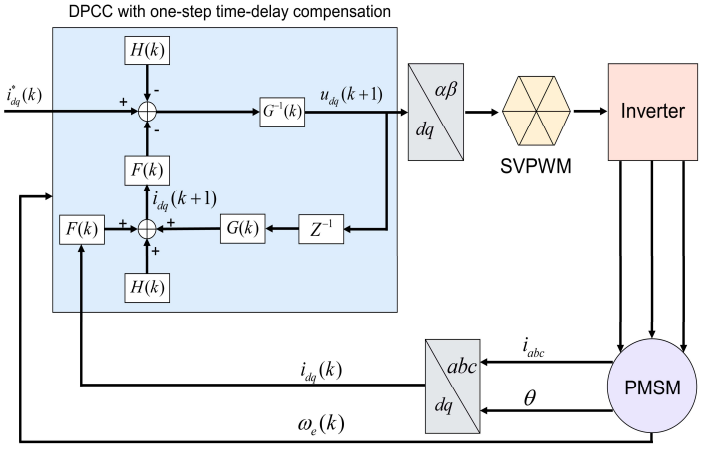

Figure 1. Diagram of delay compensation DPCC.

2.2. Parameter Mismatch Error Analysis

In the practical running of a motor, there will be phenomena such as temperature increases and flux linkage saturation [9] which will lead to the controller parameters being different from the actual parameters of the motor, and this will then generate a steady-state error.

The parameters in the predictive model of (5) are fixed and expressed as L_0, R_0, and ψ_{f0}. The practical parameters of the motor under various working conditions are expressed as L_s, R_s, and ψ_f. Therefore, (5) can be rewritten as follows:

$$\begin{bmatrix} u_d(k) \\ u_q(k) \end{bmatrix} = {G_0}^{-1}\left\{ \begin{bmatrix} i^*_d(k+1) \\ i^*_q(k+1) \end{bmatrix} - F_0(k) \begin{bmatrix} i_d(k) \\ i_q(k) \end{bmatrix} - H_0(k) \right\} \tag{7}$$

where $G_0 = \begin{bmatrix} \frac{T_s}{L_0} & 0 \\ 0 & \frac{T_s}{L_0} \end{bmatrix}$, $F_0(k) = \begin{bmatrix} 1 - \frac{T_s R_0}{L_0} & T_s\omega_e(k) \\ -T_s\omega_e(k) & 1 - \frac{T_s R_0}{L_0} \end{bmatrix}$, and $H_0(k) = \begin{bmatrix} 0 \\ -\frac{T_s\psi_{f0}\omega_e(k)}{L_0} \end{bmatrix}$.

By combining (7) and (3), we obtain the following:

$$\begin{cases} i_d(k+1) = \frac{L_0}{L_s} i^*_d(k+1) + \frac{(\Delta L - \Delta R T_s)}{L_s} i_d(k) + \frac{\Delta L \omega_e(k) T_s}{L_s} i_q(k) \\ i_q(k+1) = \frac{L_0}{L_s} i^*_q(k+1) + \frac{(\Delta L - \Delta R T_s)}{L_s} i_q(k) - \frac{\Delta L \omega_e(k) T_s}{L_s} i_d(k) - \frac{\Delta\psi_f \omega_e(k) T_s}{L_s} \end{cases} \tag{8}$$

where $\Delta L = L_s - L_0$, $\Delta R = R_s - R_0$, and $\Delta\psi_f = \psi_f - \psi_{f0}$ denote the errors between the practical motor parameters and the parameters in the predictive model. With the control method of $i_d = 0$, the d-axis reference current is consistently 0. Then, from (8), we obtain the following:

$$\begin{cases} i_d(k+1) - i^*_d(k+1) = \frac{(\Delta L - \Delta R T_s)}{L_s} i_d(k) + \frac{\Delta L \omega_e(k) T_s}{L_s} i_q(k) \\ i_q(k+1) - i^*_q(k+1) = -\frac{\Delta L}{L_s} i^*_q(k+1) + \frac{(\Delta L - \Delta R T_s)}{L_s} i_q(k) - \frac{\Delta L \omega_e(k) T_s}{L_s} i_d(k) - \frac{\Delta\psi_f \omega_e(k) T_s}{L_s} \end{cases} \tag{9}$$

According to (9), the error of the dq-axis current is associated with the inductance, the resistance errors, and the electrical angular velocity. In addition, the q-axis current error is also related to the flux linkage error.

Therefore, it is necessary to compensate for the error to solve the DPCC current static error caused by the mismatched motor parameters.

3. An Integral Sliding Mode Compensation Method with Weakened Integrals

3.1. Design of Sliding Mode Surface

The general integral sliding mode surface is shown as (10) since the relative order of the system is one in the current loop [17]:

$$S = e + K\int_0^t e d\tau \tag{10}$$

where S denotes the sliding mode surface, e denotes the error, and K denotes an adjustable coefficient. As there is an integral role in the design of the ordinary integral sliding mode surface, it will generate the integral saturation phenomenon when the system error is large, and this will lead to excessive overshooting, which is not beneficial to the system control performance [20].

Therefore, a boundary layer is introduced in the sliding mode surface in this article to weaken the integrals so as to improve the integral saturation issue. According to [21], the sliding mode surface is designed as follows:

$$\begin{cases} \dot{\rho} = -m\rho + \mu(1+\lambda)sat(\frac{S}{\mu}) - \lambda S \\ S = e + m\rho \end{cases} \tag{11}$$

where $sat(\frac{S}{\mu}) = \begin{cases} \frac{S}{\mu}, |S| \le \mu \\ \mathrm{sgn}(S), |S| > \mu \end{cases}$ is the saturation function, $\mathrm{sgn}(S)$ denotes the sign function of the sliding mode surface, $\mu > 0$ indicates the range of the boundary layer thickness, and $\lambda \ge -1$ is the regulatory factor of the degree of integral weakening. According to the relationship between the sliding mode surface and the boundary layer thickness, it is divided into the following three conditions:

When $|S| \le \mu$,

$$\dot{\rho} = -m\rho + S(1+\lambda) - \lambda S = e \tag{12}$$

When $S > \mu$,

$$\dot{\rho} = -m\rho + \mu(1+\lambda) - \lambda S = e - (1+\lambda)(S-\mu) = e - (1+\lambda)(|S|-\mu) \tag{13}$$

When $S < -\mu$,

$$\dot{\rho} = -m\rho - \mu(1+\lambda) - \lambda S = e - (1+\lambda)(S+\mu) = e + (1+\lambda)(|S|-\mu) \tag{14}$$

From (11)–(14), it can be seen that $\dot{\rho} = e$ plays the role of the conventional integral inside the boundary layer, and the integral is weakened outside the boundary layer. The degree of weakening hinges on $(1+\lambda)(|S|-\mu)$, which is associated with the error between the absolute value of the sliding mode surface and the boundary layer thickness, as well as the regulatory factor λ [21]. When the boundary layer thickness is certain, λ can also be adjusted to find the appropriate degree of weakening.

3.2. Weakened Integral Sliding Mode Compensation Method

Equation (2) can be rewritten as follows when considering only the model parameter errors:

$$\begin{cases} \frac{di_d}{dt} = \frac{1}{L_0}u_d - \frac{R_0}{L_0}i_d + \omega_e i_q + f_d \\ \frac{di_q}{dt} = \frac{1}{L_0}u_q - \frac{R_0}{L_0}i_q - \omega_e i_d - \frac{\psi_f \omega_e}{L_0} + f_q \\ f_d = \left(\frac{1}{L_s} - \frac{1}{L_0}\right)u_d - \left(\frac{R_s}{L_s} - \frac{R_0}{L_0}\right)i_d \\ f_q = \left(\frac{1}{L_s} - \frac{1}{L_0}\right)u_q - \left(\frac{R_s}{L_s} - \frac{R_0}{L_0}\right)i_q - \left(\frac{\psi_f}{L_s} - \frac{\psi_{f0}}{L_0}\right)\omega_e \end{cases} \tag{15}$$

where f_d and f_q denote disturbances owing to parameter mismatches.

The main idea of this compensation control method is that the output voltage is divided into two parts, $u = u_0 + u_1$, where u_0 denotes the predictive voltage of the delayed compensation DPCC, which is the main control quantity, and u_1 denotes the compensation voltage, which suppresses any disturbance.

In the case of a very short current control period, the current error is set to the following:

$$\begin{bmatrix} e_d \\ e_q \end{bmatrix} = \begin{bmatrix} i_d(k+1) - i_d^*(k) \\ i_q(k+1) - i_q^*(k) \end{bmatrix} \tag{16}$$

where $i_d^*(k)$ and $i_q^*(k)$ are the dq-axis reference currents at the kth moment. Therefore, the sliding mode surface is designed as follows:

$$\begin{bmatrix} S_d \\ S_q \end{bmatrix} = \begin{bmatrix} e_d + m\rho \\ e_q + m\rho \end{bmatrix} \tag{17}$$

By combining (2) and (15) to take the derivative for the sliding mode surface, we obtain the following:

$$\dot{S} = \begin{bmatrix} \dot{S}_d \\ \dot{S}_q \end{bmatrix} = \begin{bmatrix} \frac{u_d - u_{d0}}{L_0} + f_d + m\dot{\rho}_d \\ \frac{u_q - u_{q0}}{L_0} + f_q + m\dot{\rho}_q \end{bmatrix} = \begin{bmatrix} \frac{u_{d1}}{L_0} + f_d + m\dot{\rho}_d \\ \frac{u_{q1}}{L_0} + f_q + m\dot{\rho}_q \end{bmatrix} \tag{18}$$

The reaching law adopts the following, which adds the absolute value of the sliding mode surface to the isochronous reaching term of the conventional exponential reaching law. When the motion state of a system is further away from the surface, the reaching speed is higher, and when it is closer to the surface, the speed is lower; this can enable a smoother entry into the sliding mode surface and simultaneously weaken chattering [22].

$$\dot{S} = -\varepsilon|S|\mathrm{sgn}(S) - \alpha S \tag{19}$$

where $\varepsilon > 0$ and $\alpha > 0$.

By combining (18) and (19), we obtain the control law, which is also the dq-axis compensation voltage:

$$u_1 = \begin{bmatrix} u_{d1} \\ u_{q1} \end{bmatrix} = \begin{bmatrix} L_0(-\varepsilon|S_d|\mathrm{sgn}(S_d) - \alpha S_d) - L_0 m\dot{\rho}_d \\ L_0(-\varepsilon|S_q|\mathrm{sgn}(S_q) - \alpha S_q) - L_0 m\dot{\rho}_q \end{bmatrix} \tag{20}$$

3.3. Stability Analysis

To judge whether the system satisfies the sliding mode surface reachability and stability, the Lyapunov function was selected in accordance with the Lyapunov stability theory:

$$V = \frac{S^2}{2} \tag{21}$$

$$\dot{V} = S\dot{S} = S(\frac{u_1}{L_0} + f + m\dot{\rho}) = S(f - \varepsilon|S|\mathrm{sgn}(S) - \alpha S) \tag{22}$$

When $S > 0$, we made $\dot{V} = S(f - \varepsilon S - \alpha S) < 0$ and obtained $\varepsilon > \frac{f}{S} - \alpha$.

When $S < 0$, we made $\dot{V} = S(f - \varepsilon S - \alpha S) < 0$ and obtained $\varepsilon > \frac{f}{S} - \alpha$.

In summary, $\dot{V}$ is always negative when $\varepsilon > \frac{f}{S} - \alpha$, and $\dot{V} = 0$ only when $S = 0$, which proves that the system is stable. Even if the system parameters are mismatched or disturbed by other factors, this reaching law enables the system to reach the surface for sliding mode motion and makes the system stable.

3.4. Adding Weight Factors to Optimize Feedback Currents and Solve the Inductance Mismatch Problem

The system will be unstable and the feedback current will fluctuate widely when the predictive model inductance is more than twice the actual motor value. Therefore, in this article, the feedback current was corrected by introducing weight factors in accordance with [23]:

$$\bar{i}_{dq}(k) = xi^*_{dq}(k) + iy_{dq}(k) \tag{23}$$

where $x + y = 1$, $0 < x < 1$, and $0 < y < 1$; $\bar{i}_{dq}(k)$ denotes the corrected feedback current of the dq-axis; and $i_{dq}(k)$ is the dq-axis feedback current before correction.

In the case of a very short current control period, (23) and (8) are combined and simplified to obtain the following:

$$\begin{cases} i_d(k+1) - i^*_d(k+1) = \frac{\Delta L\omega_e(k)T_s}{L_0(1-x)}\left[x\Delta i_q(k) + i_q(k)\right] \\ i_q(k+1) - i^*_q(k+1) = -\frac{\Delta L\omega_e(k)T_s}{L_0(1-x)}\left[x\Delta i_d(k) + i_d(k)\right] - \frac{\Delta\psi_f\omega_e(k)T_s}{L_0(1-x)} \end{cases} \tag{24}$$

where $\Delta i_d(k) = i^*_d(k) - i_d(k)$ and $\Delta i_q(k) = i^*_q(k) - i_q(k)$.

From (24), it can be seen that the problem of large current fluctuations due to the excessive inductance of the predictive model can be reduced, but the size of the weight factor also affects the dq-axis steady-state error, which can be compensated by the algorithm, as mentioned above. Figure 2 shows the structure of the optimized method according to which a weakened integral sliding mode is combined with robust control.

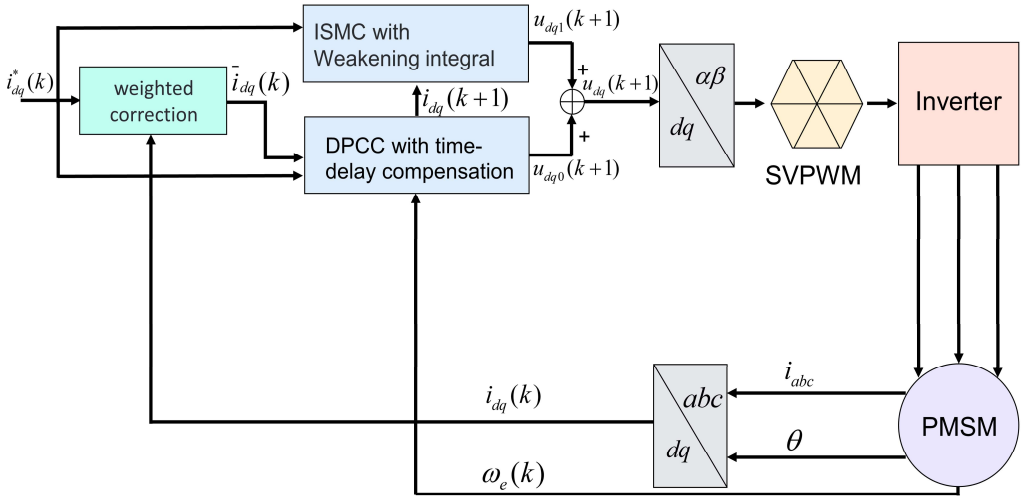

Figure 2. Structure of method according to which a weakened integral sliding mode is combined with weighting factors.

4. Simulation Study

To verify the effectiveness of this paper's theory in error compensation and weakening overshoot, a control simulation model was built in MATLAB/Simulink R2022a for a simulation analysis. The relevant SPMSM parameters are listed in Table 1. Because the motor parameters cannot be changed artificially in practice, the mismatches in the parameters of the actual motor caused by external influences were simulated by changing the predictive model motor parameters. Further, the DPCC method used in the simulations and in the experiment was one-step delay compensation DPCC.

Table 1. SPMSM parameters.

Parameter	Value
Rated voltage (V)	220
Rated speed (rpm)	3000
Rated torque (Nm)	2.4
Number of pole pairs	4
dq-axis inductance (mH)	5
Stator resistance (Ω)	1.08
Flux linkage (Wb)	0.0819

The conditions of the simulation were set as follows: the control frequencies of the current and speed loop were 10 kHz and 1 kHz, respectively. The DC voltage source was set to 60 V, and the weight factors were $x = y = 0.5$.

In order to demonstrate the effects of adding weight factors under a mismatch of the inductance parameters, a simulation of the inductance mismatch ($L_0 = 2L_s$) of the predictive model was set under the following conditions: the rotational speed was 450 rpm and the load torque increased from 0 to 1 Nm at 0.2 s and decreased from 1 to 0 Nm at 0.4 s when the weight factors were $x = y = 0.5$. Figure 3a shows that the dq-axis feedback current under DPCC undergoes obvious fluctuations, while Figure 3b shows that the dq-axis feedback current does not undergo obvious fluctuations after weight factors are added. This shows that the impact generated by the inductance mismatch is suppressed, but it also shows the generation of certain steady-state errors.

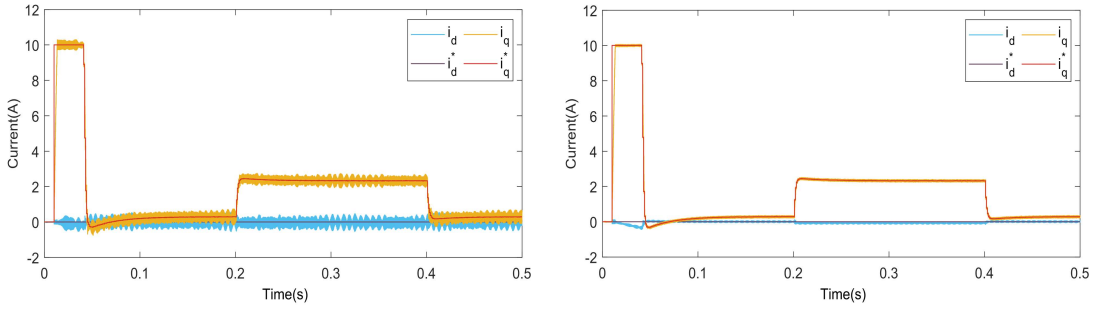

(**a**) (**b**)

Figure 3. Comparison of dq-axis current simulations of two methods at 450 rpm with torque variation (1 Nm) in case of inductance mismatch ($L_0 = 2L_s$): (**a**) DPCC; (**b**) DPCC with weight factors.

Simulation tests of the current loop were carried out to demonstrate that the weakened integral sliding mode structure improves the integral saturation and reduces the overshoot. The simulation conditions were such that the q-axis reference current increased from 0 to 3 A at 0.1 s. Figures 4–6 represent the q-axis feedback and the reference currents when the three parameters of the model, namely inductance, resistance, and flux linkage, were not mismatched as well as when they were simultaneously mismatched. Figures 4a, 5a and 6a indicate the q-axis feedback and the reference currents of the normal integral sliding mode optimization combined with the weight factors, and Figures 4b, 5b and 6b indicate the q-axis feedback

and the reference currents of the weakened integral sliding mode optimization combined with the weight factors. Moreover, methods (a) and (b) differ from each other only in the construction of the sliding mode surface. It can be seen in (a) that current overshooting occurs during current variation, while it is clear that in (b) the weakened integral sliding mode structure suppresses this phenomenon well.

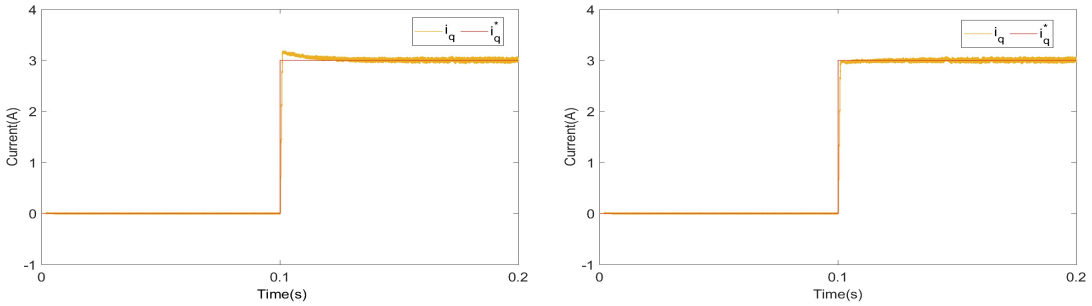

(**a**) (**b**)

Figure 4. Comparison of q- axis current simulations of two methods with current variations (0 A to 3 A) and without parameter mismatches ($R_0 = R_s$, $L_0 = L_s$, and $\psi_{f0} = \psi_f$): (**a**) DPCC with normal integral sliding mode compensation combined with weight factors; (**b**) DPCC with weakened integral sliding mode compensation combined with weight factors.

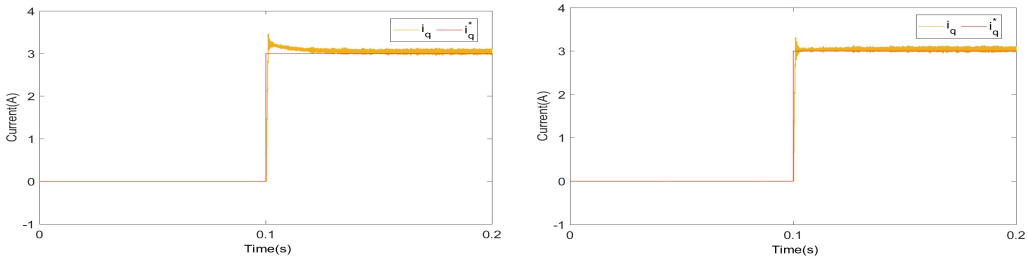

(**a**) (**b**)

Figure 5. Comparison of q-axis current simulations of two methods with current variations (0 A to 3 A) and with simultaneous resistance, inductance, and flux linkage mismatches ($R_0 = 2R_s$, $L_0 = 2L_s$, and $\psi_{f0} = 2\psi_f$): (**a**) DPCC with normal integral sliding mode compensation combined with weight factors; (**b**) DPCC with weakened integral sliding mode compensation combined with weight factors.

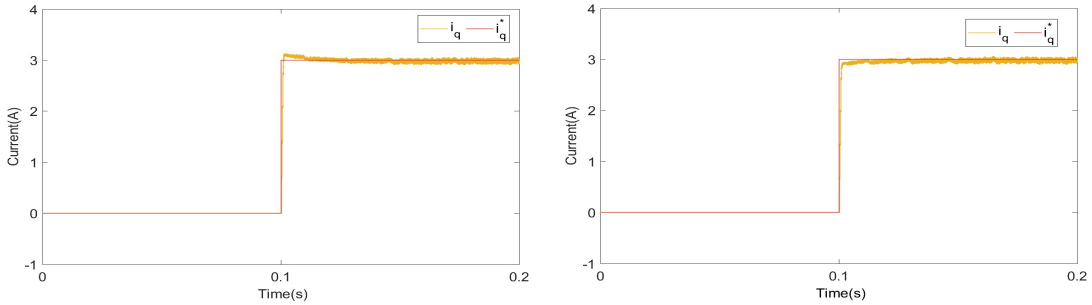

(**a**) (**b**)

Figure 6. Comparison of q-axis current simulations of two methods with current variations (0 A to 3 A) and with simultaneous resistance, inductance, and flux linkage mismatches ($R_0 = 0.75R_s$, $L_0 = 0.75L_s$, and $\psi_{f0} = 0.75\psi_f$): (**a**) DPCC with normal integral sliding mode compensation combined with weight factors; (**b**) DPCC with weakened integral sliding mode compensation combined with weight factors.

Figures 7–9 represent comparisons of simulations about dq-axis currents between DPCC and DPCC optimized with weakened integral sliding mode compensation combined

with weight factors in which the rotational speed is 450 rpm and the load torque increases from 0 to 1 Nm at 0.2 s and decreases from 1 to 0 Nm at 0.4 s, and with single parameter mismatches. Figure 7 shows the case of resistance mismatch, and we can see from Figure 7a,c that when $R_0 = 2R_s$, the q-axis feedback value is slightly larger than the reference current for DPCC, with an error of about 4.4% of the q-axis reference when loaded, and that when $R_0 = 0.5R_s$, it is slightly smaller than the reference current, with an error of about 2.1% of the q-axis reference when loaded. From Figure 7b,d, it is evident that the method proposed in this article can remove steady-state errors. Figure 8 represents the case of inductance mismatch. Figure 8a shows that the dq-axis feedback current fluctuates widely for DPCC when $L_0 = 2L_s$, and that the range of fluctuation is about 0.3 A, which is about 12.7% of the q-axis reference when loaded. Figure 8b shows that the dq-axis current fluctuates very little after being optimized and compensated, i.e., about 2.6% of the q-axis reference when loaded. When $L_0 = 0.5L_s$, as is shown in Figure 8c, it has a large impact on the d-axis of the DPCC, and its steady-state error is about 0.13 A when loaded. The steady-state error can be eliminated with compensation, as is shown in Figure 8d. Figure 9 represents a flux linkage mismatch, and from Figure 9a,c, it is clear that for DPCC the q-axis feedback value exceeds the reference when $\psi_{f0} = 2\psi_f$, and that the error of both is about 35% of the q-axis reference when loaded, whereas the q-axis feedback value is less than the reference when $\psi_{f0} = 0.5\psi_f$, and the error of both is about 11.4% of the q-axis reference when loaded. From Figure 9b,d, it is clear that the error can be eliminated after compensation.

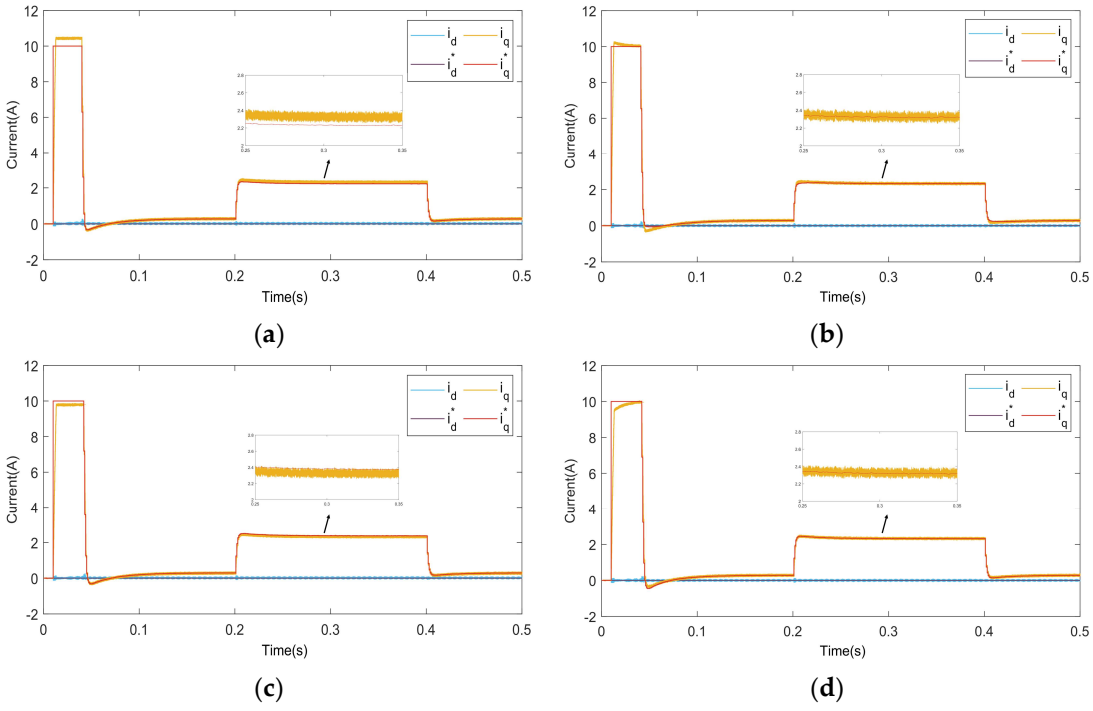

Figure 7. Comparison of dq-axis current simulations of two methods at 450 rpm with resistance mismatch under torque variation (1 Nm): (**a**,**b**) $R_0 = 2R_s$; (**c**,**d**) $R_0 = 0.5R_s$; (**a**,**c**) DPCC; (**b**,**d**) DPCC with weakened integral sliding mode compensation combined with weight factors.

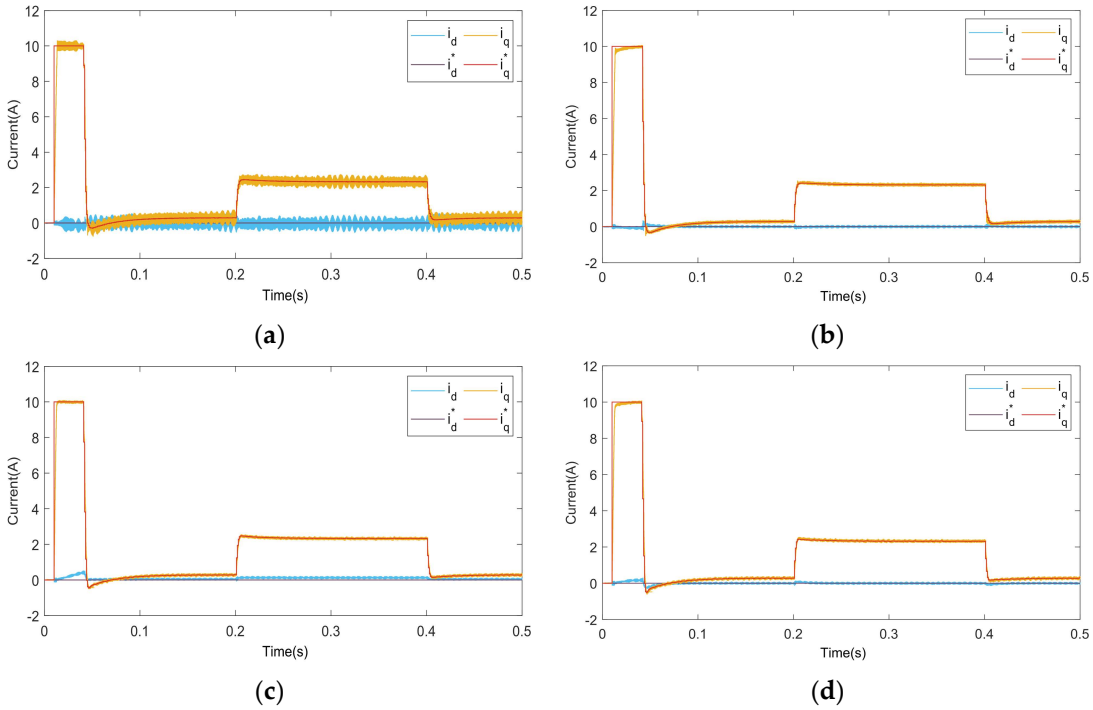

Figure 8. Comparison of dq-axis current simulations of two methods at 450 rpm with torque variation (1 Nm) for inductance mismatch: (**a**,**b**) $L_0 = 2L_s$; (**c**,**d**) $L_0 = 0.5L_s$; (**a**,**c**) DPCC; (**b**,**d**) DPCC with weakened integral sliding mode compensation combined with weight factors.

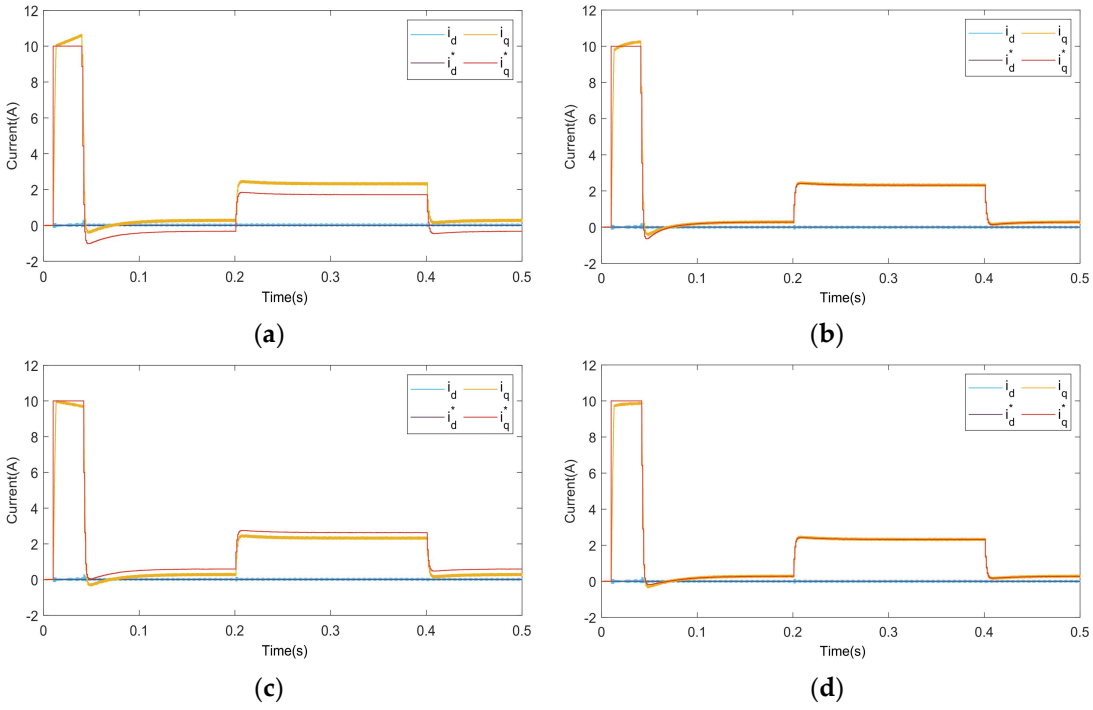

Figure 9. Comparison of dq-axis current simulations of two methods at 450 rpm with torque variation (1 Nm) for flux linkage mismatch. (**a**,**b**) $\psi_{f0} = 2\psi_f$; (**c**,**d**) $\psi_{f0} = 0.5\psi_f$; (**a**,**c**) DPCC; (**b**,**d**) DPCC with weakened integral sliding mode compensation combined with weight factors.

Figures 10 and 11 represent comparisons of simulations about dq-axis currents between DPCC and DPCC optimized with weakened integral sliding mode compensation combined with weight factors under a rotational speed of 450 rpm and a load torque that increases

from 0 to 1 Nm at 0.2 s and decreases from 1 to 0 Nm at 0.4 s, and for which the three parameters of resistance, inductance, and flux linkage are simultaneously mismatched. It can be shown that the proposed method can effectively eliminate the error and suppress the disturbance.

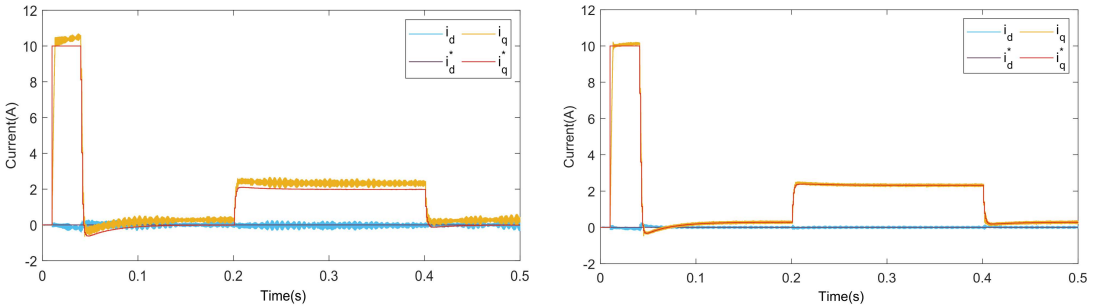

(**a**) (**b**)

Figure 10. Comparison of dq-axis current simulations of two methods at 450 rpm with torque variation (1 Nm) under simultaneous resistance, inductance, and flux linkage mismatches ($R_0 = 2R_s$, $\psi_{f0} = 2\psi_f$, and $L_0 = 2L_s$): (**a**) DPCC; (**b**) DPCC with weakened integral sliding mode compensation combined with weight factors.

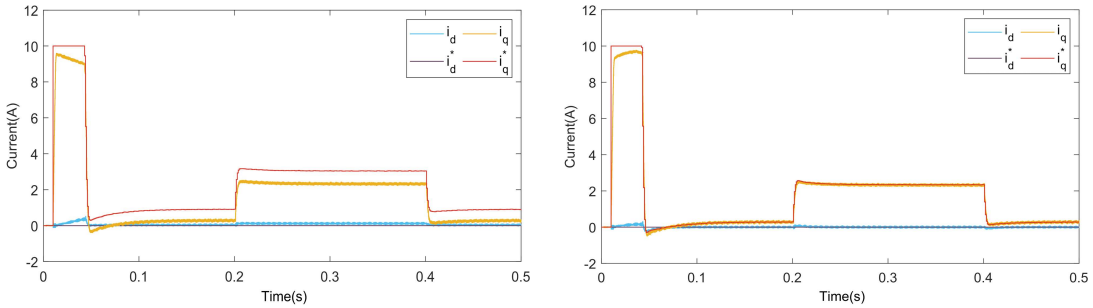

(**a**) (**b**)

Figure 11. Comparison of dq-axis current simulations of two methods at 450 rpm with torque variation (1 Nm) under simultaneous resistance, inductance, and flux linkage mismatches ($R_0 = 0.5R_s$, $\psi_{f0} = 0.5\psi_f$, and $L_0 = 0.5L_s$): (**a**) DPCC; (**b**) DPCC with weakened integral sliding mode compensation combined with weight factors.

In conclusion, the comparison results of the simulations indicate that the DPCC method combining the weakened integral sliding mode compensation with weight factors has lower parameter sensitivity, which considerably enhances current immunity.

5. Experimental Study

To demonstrate the effectiveness of the method involving weakened integral sliding mode compensation combined with weight factors suggested by the simulation, an experiment was performed using the PMSM experimental platform, shown in Figure 12, with a 750 W SPMSM. The motor electrical parameters are listed in Table 1. The power supply used a 60 V DC voltage source, the control board and the driver board used 24 V voltage input, the DSP control chip selected was a TMS320F28335, the PWM frequency was 10 kHz, the frequency of the speed loop was 1 kHz, the M method was used to measure the motor speed, the dead time was 3.2 us, and the weight factors were set as $x = y = 0.5$.

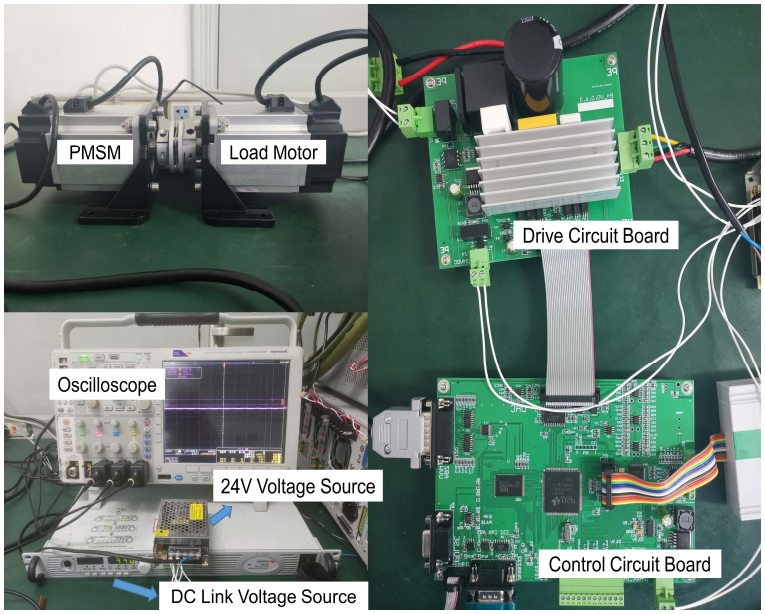

Figure 12. PMSM experimental platform.

With the purpose of proving the effectiveness of introducing weight factors to suppress current fluctuation, the experiment was designed on the basis of the simulation. The DC voltage was set to 60 V, the rotational speed was set to 450 rpm, the load torque increased from 0.2 to 0.5 Nm at 0.5 s and then decreased from 0.5 to 0.2 Nm at 3.5 s, and the model inductance value was 1.4 times the stator inductance of the motor ($L_0 = 1.4L_s$). Figure 13a shows a large fluctuation in the dq-axis current in DPCC, which leads to system instability, while Figure 13b adds weight factors to DPCC, which can greatly reduce the current fluctuations, but which produce a certain amount of steady-state error.

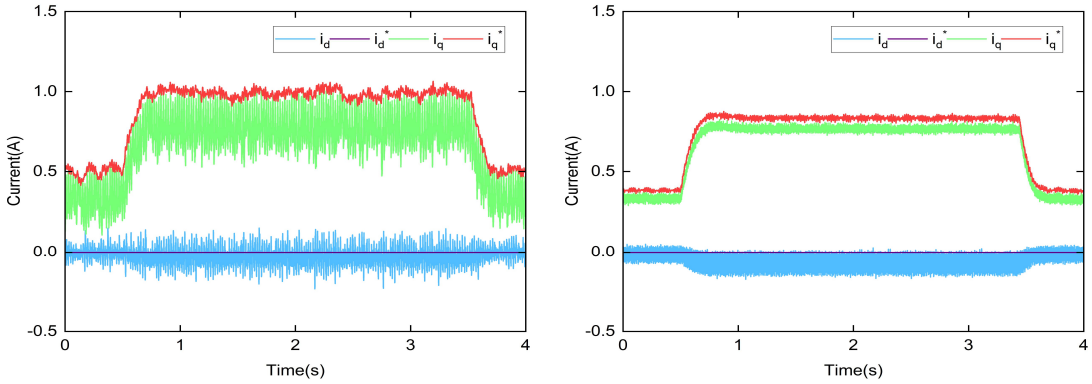

Figure 13. Experimental comparison of dq-axis currents of two methods at 450 rpm with torque variation (0.2 to 0.5 to 0.2 Nm) under inductance mismatch conditions ($L_0 = 1.4L_s$): (**a**) DPCC; (**b**) DPCC with weight factors.

To effectively verify the feasibility of the anti-integral saturation of the weakened integral sliding mode, the current loop experiment was set up according to the simulation and the q-axis reference current was increased from 0 to 1.5 A at 0.05 s. Figures 14–16 indicate that the three parameters of the model were 1, 1.5, and 0.75 times the motor parameters, respectively, where current loops (a) and (b) were both optimized via DPCC using the sliding mode compensation and weight factors, and they differed only in their surface selection, with (a) using the ordinary integral sliding mode surface and (b) using the weakened integral sliding mode surface. As is shown in Figure 14, when there were no

parameter mismatches, the overshoot of (a) was about 65.3% of the steady-state reference value, and the time to restore stability was about 0.012 s, while the overshoot of (b) was about 3.3% of the steady-state reference value, and the time to restore stability was about 0.006 s. Figure 15 shows that when the three parameters of the model were simultaneously changed to 1.5 times their actual values, the overshoot of (a) was about 53.3% of the steady-state reference value, and the time to restore stability was about 0.013 s, while the overshoot of (b) was about 4.3% of the steady-state reference value, and the time to restore stability was about 0.013 s. As can be seen in Figure 16, when the three parameters of the model were simultaneously changed to 0.75 times their actual values, the overshoot of (a) was about 67.3% of the steady-state reference value, and the time to return to stability was about 0.015 s, while (b) hardly produced any overshooting, and the time to return to stability was about 0.008 s. In terms of the time required to first achieve a steady-state value, it can be seen from the above three situations that (b) takes longer than (a). In terms of overshooting and the time needed to restore stability, it is clear that the weakened integral sliding mode surface not only weakens the overshoot due to the introduction of the integral term when the currents change, but that it also shortens the time required to reach a steady state.

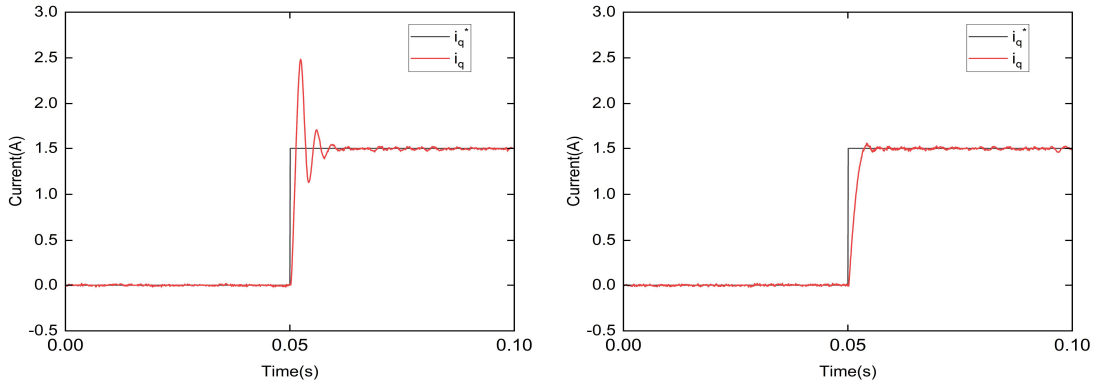

Figure 14. Experimental comparison of q-axis currents of two methods under current variation (0 A to 1.5 A) without parameter mismatches ($R_0 = R_s$, $L_0 = L_s$, and $\psi_{f0} = \psi_f$): (**a**) DPCC with normal integral sliding mode compensation combined with weight factors; (**b**) DPCC with weakened integral sliding mode compensation combined with weight factors.

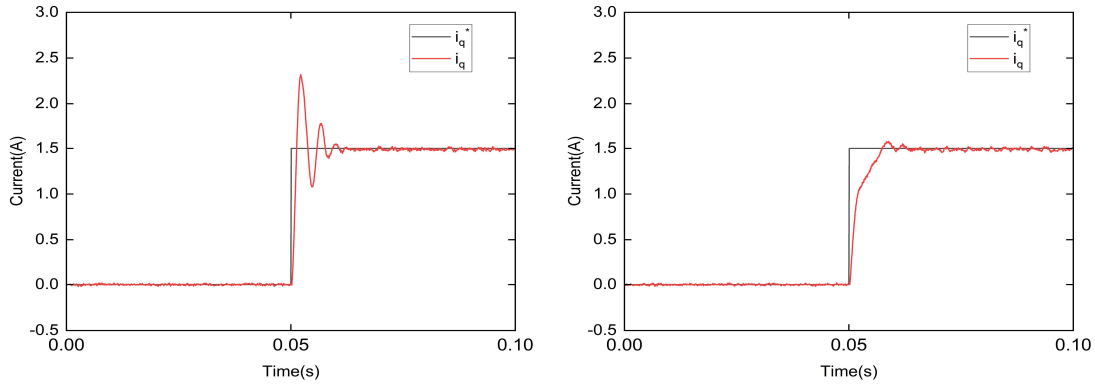

Figure 15. Experimental comparison of q-axis currents of two methods under current variation (0 A to 1.5 A) with simultaneous mismatches of three parameters ($R_0 = 1.5R_s$, $L_0 = 1.5L_s$, and $\psi_{f0} = 1.5\psi_f$). (**a**) DPCC with normal integral sliding mode compensation combined with weight factors; (**b**) DPCC with weakened integral sliding mode compensation combined with weight factors.

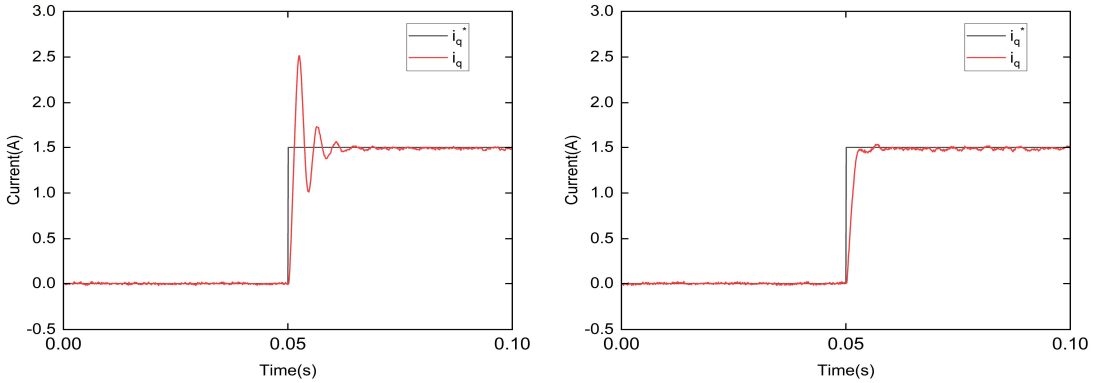

(**a**) (**b**)

Figure 16. Experimental comparison of q-axis currents of two methods under current variation (0 A to 1.5 A) with simultaneous mismatches of three parameters ($R_0 = 0.75R_s$, $L_0 = 0.75L_s$, and $\psi_{f0} = 0.75\psi_f$). (**a**) DPCC with normal integral sliding mode compensation combined with weight factors; (**b**) DPCC with weakened integral sliding mode compensation combined with weight factors.

Figures 17–22 show the load variation experiment based on the simulation in which the dq-axis current variations of DPCC and DPCC with weakened integral sliding mode compensation combined with weight factor optimization are compared in the case of parameter mismatching. In the experiment, the DC voltage was set to 60 V, the rotational speed was 450 rpm, and the load torque increased from 0.2 to 0.5 Nm at 0.5 s and then decreased from 0.5 to 0.2 Nm at 3.5 s.

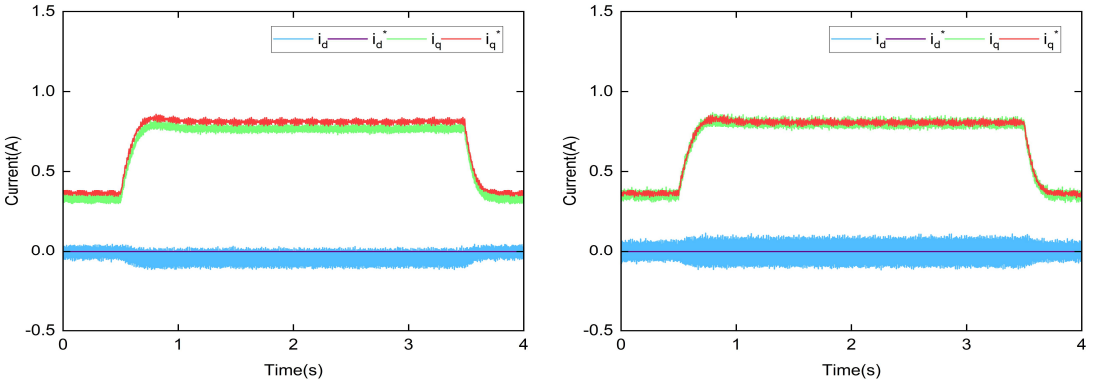

(**a**) (**b**)

Figure 17. Experimental comparison of dq-axis currents at 450 rpm with torque variation (0.2 to 0.5 to 0.2 Nm) and without parameter mismatches ($R_0 = R_s$, $\psi_{f0} = \psi_f$, and $L_0 = L_s$): (**a**) DPCC; (**b**) DPCC with weakened integral sliding mode compensation combined with weight factors.

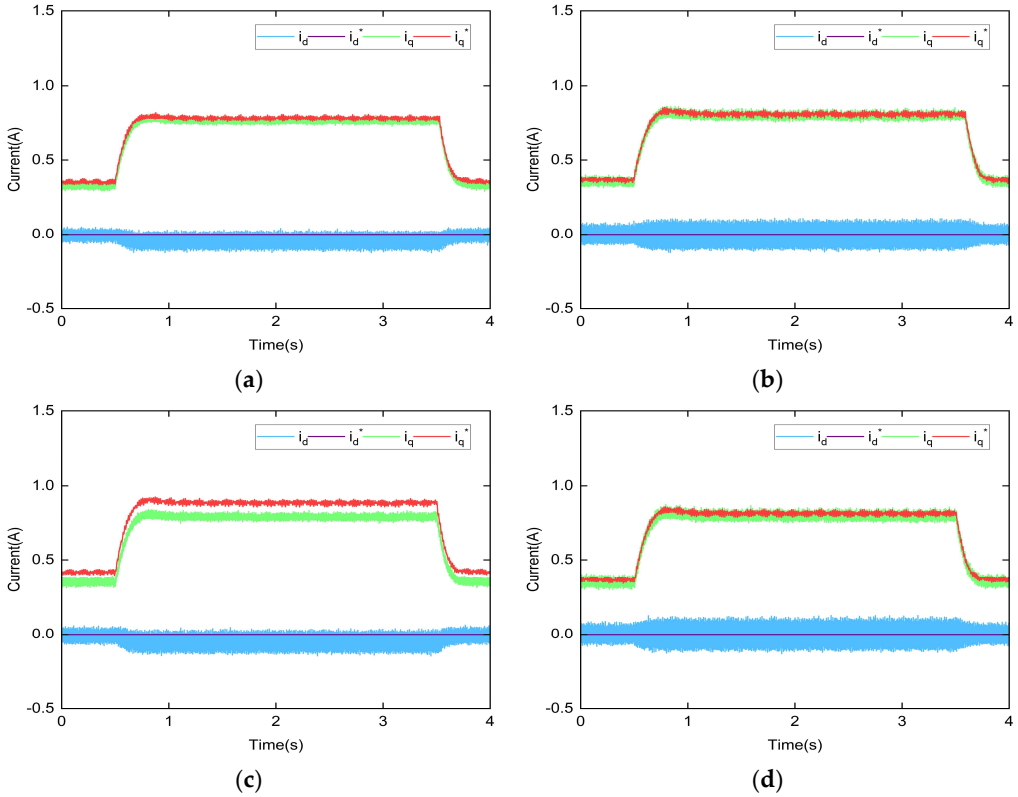

Figure 18. Experimental comparison of dq-axis currents at 450 rpm with torque variation (0.2 to 0.5 to 0.2 Nm) and resistance mismatch: (**a**,**b**) $R_0 = 2R_s$; (**c**,**d**) $R_0 = 0.5R_s$; (**a**,**c**) DPCC; (**b**,**d**) DPCC with weakened integral sliding mode compensation combined with weight factors.

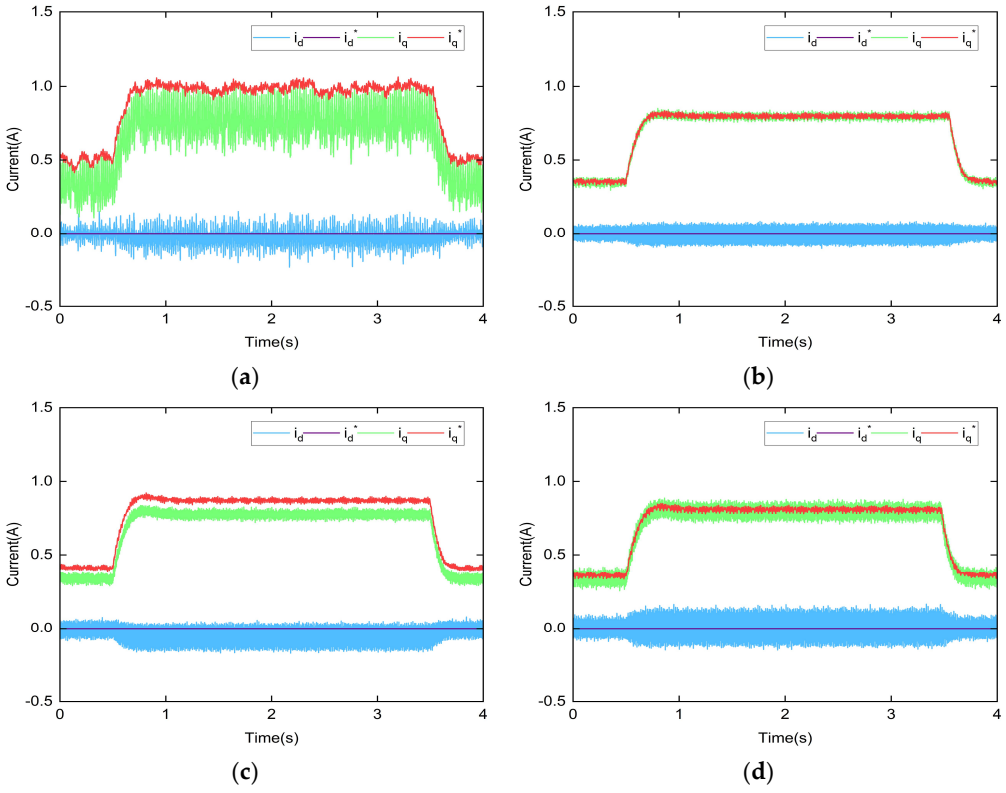

Figure 19. Experimental comparison of dq-axis currents at 450 rpm with torque variation (0.2 to 0.5 to 0.2 Nm) and inductance mismatch: (**a**,**b**) $L_0 = 1.4L_s$; (**c**,**d**) $L_0 = 0.5L_s$; (**a**,**c**) DPCC; (**b**,**d**) DPCC with weakened integral sliding mode compensation combined with weight factors.

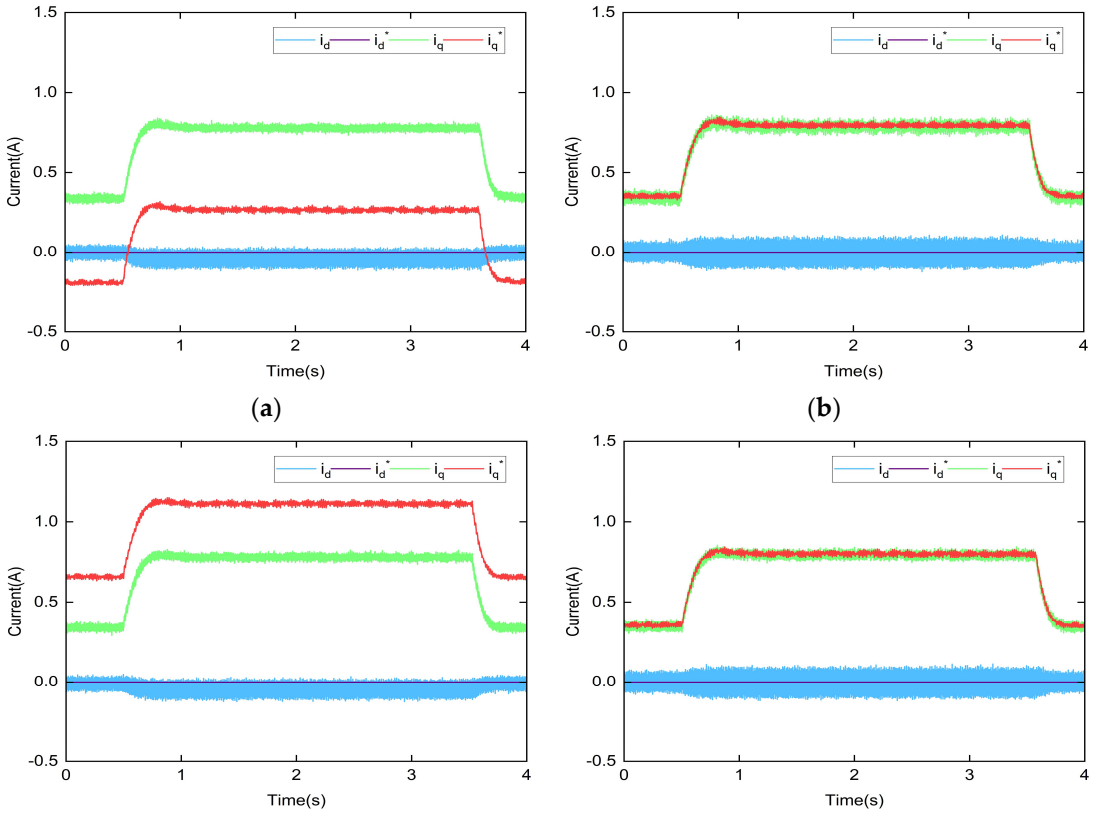

Figure 20. Experimental comparison of dq-axis currents at 450 rpm with torque variation (0.2 to 0.5 to 0.2 Nm) and flux linkage mismatch: (**a**,**b**) $\psi_{f0} = 2\psi_f$; (**c**,**d**) $\psi_{f0} = 0.5\psi_f$; (**a**,**c**) DPCC; (**b**,**d**) DPCC with weakened integral sliding mode compensation combined with weight factors.

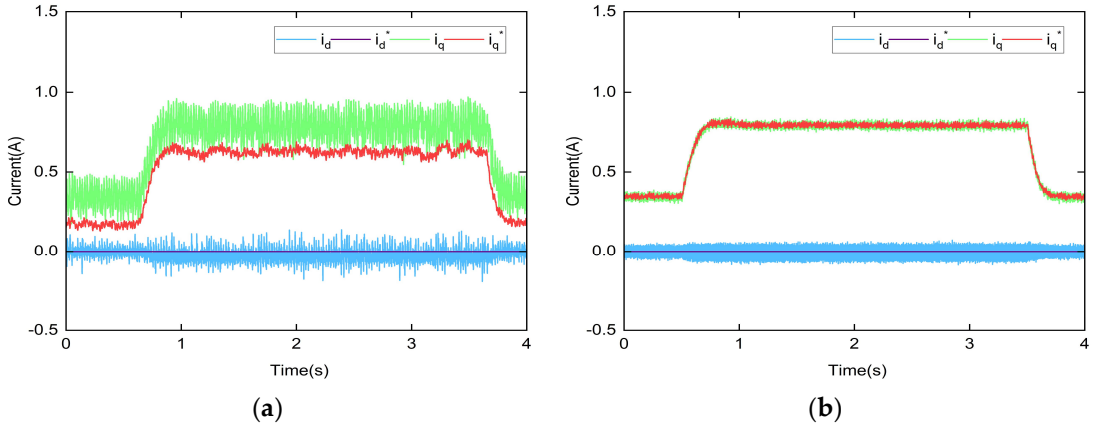

Figure 21. Experimental comparison of dq-axis currents at 450 rpm with torque variation (0.2 to 0.5 to 0.2 Nm) and simultaneous resistance, inductance, and flux linkage mismatches ($R_0 = 2R_s$, $\psi_{f0} = 2\psi_f$, and $L_0 = 2L_s$): (**a**) DPCC; (**b**) DPCC with weakened integral sliding mode compensation combined with weight factors.

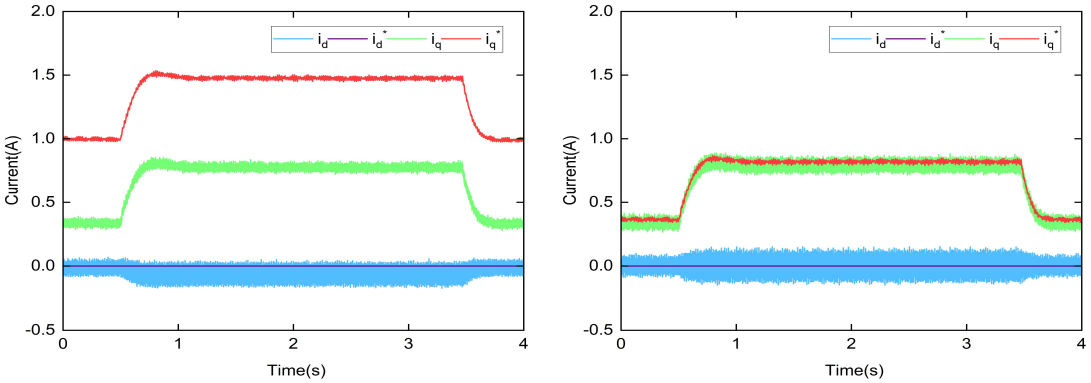

Figure 22. Experimental comparison of dq-axis currents at 450 rpm with torque variation (0.2 to 0.5 to 0.2 Nm) and simultaneous resistance, inductance, and flux linkage mismatches ($R_0 = 0.5R_s$, $\psi_{f0} = 0.5\psi_f$, and $L_0 = 0.5L_s$): (**a**) DPCC; (**b**) DPCC with weakened integral sliding mode compensation combined with weight factors.

Figure 17 shows the dq-axis currents with no parameter mismatches. As is shown in Figure 17a, a slight error is produced between the dq-axis feedback and the reference current under DPCC due to the nonlinear characteristics of the practical control system as well as the influence of delayed effects, such as the inverter. This causes the d-axis feedback current to shift in the negative direction after the load is increased to a certain degree at this speed, owing to the voltage limitation of the DC supply in the experiment. Figure 17b shows that the improved method under the same conditions can overcome the factors mentioned above and can eliminate the effects of external factors, thus eliminating errors.

Figures 18–20 indicate the dq-axis currents under single motor parameter mismatches. Figure 18 represents a resistance mismatch, while Figure 18a,c show that the q-axis feedback current increases modestly when the model resistance value becomes larger ($R_0 = 2R_s$) and drops slightly when the model value is smaller than the practical resistance value ($R_0 = 0.5R_s$). Figure 18b,d show that the optimized method can compensate for the error. Figure 19 shows an inductance mismatch in which the fluctuation of the dq-axis feedback current under DPCC is clearly shown to increase when the model value is larger than the actual motor inductance value ($L_0 = 1.4L_s$), as in Figure 19a, while the model of the optimized method is shown to attenuate the current fluctuation in Figure 19b. In Figure 19c, when the model inductance changes to a smaller value ($L_0 = 0.5L_s$), the fluctuation of the d-axis feedback current under the DPCC method increases slightly, within a range of approximately 0.17 A from the negative direction, and it affects the q-axis error. In Figure 19d, the range of the negative direction of the d-axis feedback current under the optimized method is approximately 0.12 A, and this method reduces the dq-axis error. Figure 20 shows a situation in which there is a flux linkage mismatch, and Figure 20a,c show that a huge deviation is caused between the q-axis feedback and the reference current when the model flux linkage is 2, which is 0.5 times the actual motor value. Figure 20b,d show that the optimized method can compensate for the error and reduce system sensitivity to this parameter.

Figures 21 and 22 represent the dq-axis currents for a case in which the three motor parameters are simultaneously mismatched. Figure 21a shows the dq-axis current under DPCC when the model values are changed to 2 times the practical parameters ($L_0 = 2L_s$, $\psi_{f0} = 2\psi_f$, and $R_0 = 2R_s$) simultaneously, and it can be seen that the waveform is obviously fluctuating and generating a fairly big steady-state error. The optimized method in shown in Figure 21b can effectively reduce the fluctuations and compensate for the error under the same conditions. Figure 22a shows the dq-axis current under DPCC when the predictive model parameters are changed to 0.5 times their actual values ($L_0 = 0.5L_s$, $\psi_{f0} = 0.5\psi_f$,

and $R_0 = 0.5R_s$) concurrently, and it can be seen from Figure 22b that the optimized method can effectively compensate for the error under the same conditions.

According to the above results and analyses, the DPCC method which uses weakened integral sliding mode compensation combined with weight factors for optimization can not only suppress the errors and fluctuations generated by mismatches in the motor parameters, but it can also weaken the impacts of external factors and significantly improve the robustness of the system.

6. Conclusions

This article analyzes the motor parameter mismatches that generate steady-state errors in conventional DPCC and proposes a weakened integral sliding mode compensation method. This method combines the current error with the sliding mode surface and the reaching law to derive a compensation voltage to compensate for the static error. It also introduces a boundary layer in the design of the sliding mode surface to weaken the integral when the surface is outside of the boundary layer, which not only weakens the overshooting but also reduces the regulation recovery time. Secondly, weight factors are introduced to weight the feedback current to reduce fluctuations when the current fluctuation is too large and unstable due to excessive inductance mismatch. Finally, the conventional one-step delay compensation DPCC method is used to address the inherent time delay problem during the computational operation of the system. The simulation and experimental results indicate that this method can compensate for the error effectively in situations involving parameter mismatches and thereby eliminate steady-state errors, solve the problem of integral saturation, and strengthen the robustness of the system.

Author Contributions: Conceptualization, Y.Z.; methodology, Y.Z.; software, Y.Z.; validation, Y.Z.; formal analysis, Y.Z.; investigation, Y.Z.; resources, Y.Z., D.S. and C.J.; data curation, Y.Z.; writing—original draft preparation, Y.Z.; writing—review and editing, Y.Z., D.S., C.J., Q.Y. and Y.X.; visualization, Y.Z.; supervision, D.S.; project administration, D.S.; funding acquisition, D.S. All authors have read and agreed to the published version of the manuscript.

Funding: This research was funded by the Basic Science Research and Social Livelihood S&T Foundation of Nantong City in Jiangsu Province, China (Grand No. JC12022044, JC12022082, and MS22022106).

Institutional Review Board Statement: Not applicable.

Informed Consent Statement: Not applicable.

Data Availability Statement: Not applicable.

Conflicts of Interest: The authors declare no conflict of interest.

References

1. Orlowska-Kowalska, T.; Wolkiewicz, M.; Pietrzak, P.; Skowron, M.; Ewert, P.; Tarchala, G.; Krzysztofiak, M.; Kowalski, C.T. Fault Diagnosis and Fault-Tolerant Control of PMSM Drives–State of the Art and Future Challenges. *IEEE Access* **2022**, *10*, 59979–60024. [CrossRef]
2. Loganayaki, A.; Kumar, R.B. Permanent Magnet Synchronous Motor for Electric Vehicle Applications. In Proceedings of the 2019 5th International Conference on Advanced Computing & Communication Systems (ICACCS), Coimbatore, India, 15–16 March 2019; pp. 1064–1069.
3. Guo, Q.; Han, J.; Peng, W. PMSM Servo Control System Design Based on Fuzzy PID. In Proceedings of the 2017 2nd International Conference on Cybernetics, Robotics and Control (CRC), Chengdu, China, 21–23 July 2017; pp. 85–88.
4. Gao, J.; Li, S.; Xu, Y.; Zou, J. Time-Delay Compensation Method in PMSM Servo System based on Predictive Current Control with Sensitivity Analysis. In Proceedings of the 2019 22nd International Conference on Electrical Machines and Systems (ICEMS), Harbin, China, 11–14 August 2019; pp. 1–6.
5. Wang, H.; Xu, S.; Hu, H. PID Controller for PMSM Speed Control Based on Improved Quantum Genetic Algorithm Optimization. *IEEE Access* **2023**, *11*, 61091–61102. [CrossRef]
6. Lee, H.; Utkin, V.I. Chattering suppression methods in sliding mode control systems. *Annu. Rev. Control* **2007**, *31*, 179–188. [CrossRef]

7. Peng, J.; Yao, M. Overview of Predictive Control Technology for Permanent Magnet Synchronous Motor Systems. *Appl. Sci.* **2023**, *13*, 6255. [CrossRef]
8. Yang, N.; Zhang, S.; Li, X.; Li, X. A New Model-Free Deadbeat Predictive Current Control for PMSM Using Parameter-Free Luenberger Disturbance Observer. *IEEE J. Emerg. Sel. Top. Power Electron.* **2023**, *11*, 407–417. [CrossRef]
9. Yin, K.; Gao, L.; Chen, R.; Feng, Z.; Liu, S. Adaptive Deadbeat Predictive Current Control for PMSM with Feed Forward Method. *IEEE Access* **2021**, *9*, 101300–101310. [CrossRef]
10. Zhou, Y.; Zhang, S.; Zhang, C.; Li, X.; Li, X.; Yuan, X. Current Prediction Error Based Parameter Identification Method for SPMSM with Deadbeat Predictive Current Control. *IEEE Trans. Energy Convers.* **2021**, *36*, 1700–1710. [CrossRef]
11. Li, X.; Zhang, S.; Cui, X.; Wang, Y.; Zhang, C.; Li, Z.; Zhou, Y. Novel Deadbeat Predictive Current Control for PMSM with Parameter Updating Scheme. *IEEE J. Emerg. Sel. Top. Power Electron.* **2022**, *10*, 2065–2074. [CrossRef]
12. Shen, W.; Liu, H.; Shao, L. Deadbeat Predictive Current Control of Permanent Magnet Synchronous Motors Based on Disturbance Compensation. In Proceedings of the 2021 33rd Chinese Control and Decision Conference (CCDC), Kunming, China, 22–24 May 2021; pp. 4256–4263.
13. Gong, Z.; Zhang, C.; Ba, X.; Guo, Y. Improved Deadbeat Predictive Current Control of Permanent Magnet Synchronous Motor Using a Novel Stator Current and Disturbance Observer. *IEEE Access* **2021**, *9*, 142815–142826. [CrossRef]
14. Zhang, X.; Wang, Z.; Bai, H. Sliding-Mode-Based Deadbeat Predictive Current Control for PMSM Drives. *IEEE J. Emerg. Sel. Top. Power Electron.* **2023**, *11*, 962–969. [CrossRef]
15. Jiang, Y.; Xu, W.; Mu, C.; Liu, Y. Improved Deadbeat Predictive Current Control Combined Sliding Mode Strategy for PMSM Drive System. *IEEE Trans. Veh. Technol.* **2018**, *67*, 251–263. [CrossRef]
16. Wang, G.; Yang, M.; Niu, L.; Gui, X.; Xu, D. A static current error elimination algorithm for PMSM predictive current control. *Zhongguo Dianji Gongcheng Xuebao/Proc. Chin. Soc. Electr. Eng.* **2015**, *35*, 2544–2551. [CrossRef]
17. Xu, Y.; Li, S.; Zou, J. Integral Sliding Mode Control Based Deadbeat Predictive Current Control for PMSM Drives with Disturbance Rejection. *IEEE Trans. Power Electron.* **2022**, *37*, 2845–2856. [CrossRef]
18. Hu, Z.; Ding, J.; Kang, J. Deadbeat Robust Current Predictive Control for PMSM with Sliding Mode Observer. In Proceedings of the 2021 IEEE International Conference on Predictive Control of Electrical Drives and Power Electronics (PRECEDE), Jinan, China, 20–22 November 2021; pp. 622–627.
19. Zhang, X.; Hou, B.; Mei, Y. Deadbeat Predictive Current Control of Permanent-Magnet Synchronous Motors with Stator Current and Disturbance Observer. *IEEE Trans. Power Electron.* **2017**, *32*, 3818–3834. [CrossRef]
20. Qi, L.; Bao, S.; Shi, H. Permanent-magnet synchronous motor velocity control based on second-order integral sliding mode control algorithm. *Trans. Inst. Meas. Control* **2015**, *37*, 875–882. [CrossRef]
21. Li, P.; Sun, W.; Li, W. Application of improved integral sliding surface to flight control system. *Control Eng. China* **2010**, *17*, 269–271.
22. Cao, X.; Ge, Q.; Zhu, J.; Sun, P.; Wang, X. Traction-System Research of High-Speed Maglev Train Based on Integral Sliding Mode Control. *Diangong Jishu Xuebao/Trans. China Electrotech. Soc.* **2022**, *37*, 3598–3607.
23. Liu, J.; Hao, W.; Chen, A.; Tian, J. Research on Deadbeat Predictive Current Control of Permanent Magnet Synchronous Motor. *Tiedao Xuebao/J. China Railw. Soc.* **2021**, *43*, 62–72.

Disclaimer/Publisher's Note: The statements, opinions and data contained in all publications are solely those of the individual author(s) and contributor(s) and not of MDPI and/or the editor(s). MDPI and/or the editor(s) disclaim responsibility for any injury to people or property resulting from any ideas, methods, instructions or products referred to in the content.